Hydrogen in tungsten trioxide by membrane photoemission and density functional theory modeling

Emanuel Billeter [1,2] Andrea Sterzi,[1] Olga Sambalova,[1,2] René Wick-Joliat [2] Cesare Grazioli [3] Marcello Coreno [4]
Yongqiang Cheng,[5] Anibal J. Ramirez-Cuesta,[5] and Andreas Borgschulte [1,2,*]

[1]*Laboratory for Advanced Analytical Technologies, Empa - Swiss Federal Laboratories for Materials Science and Technology, Überlandstrasse 129, 8600 Dübendorf, Switzerland*
[2]*Department of Chemistry, University of Zürich, Winterthurerstrasse 190, 8057 Zürich, Switzerland*
[3]*IOM-CNR, Laboratorio TASC, Basovizza SS-14, km 163.5, 34149 Trieste, Italy*
[4]*ISM-CNR, Istituto di Struttura della Materia, LD2 Unit, 34149 Trieste, Italy*
[5]*Neutron Scattering Division, Oak Ridge National Laboratory, Oak Ridge, Tennessee 37831, USA*

The measurement of hydrogen-induced changes in the electronic structure of transition metal oxides by x-ray photoelectron spectroscopy is a challenging endeavor, since no photoelectron can be unambiguously assigned to hydrogen. The H-induced electronic structure changes in tungsten trioxide have been known for more than 100 years but are still controversially debated. The controversy stems from the difficulty in disentangling effects due to hydrogenation from the effects of oxygen deficiencies. Using a membrane approach to x-ray photoelectron spectroscopy, in combination with tunable synchrotron radiation, we measure simultaneously core levels and the valence band up to a hydrogen pressure of 1000 mbar. Upon hydrogenation, the intensities of the W^{5+} core level and a state close to the Fermi level increase following the pressure-composition isotherm curve of bulk H_xWO_3. Combining experimental data and density functional theory, the description of the hydrogen-induced coloration by a proton polaron model is corroborated. Although hydrogen is the origin of the electronic structure changes near the Fermi edge, the valence band edge is now dominated by tungsten orbitals instead of oxygen as is the case for the pristine oxide, having wider implications for its use as a (photoelectrochemical) catalyst.

I. INTRODUCTION

Hydrogen is a ubiquitous element in the environment. The element plays a key role in biology, chemistry, and physics: It is involved in numerous chemical reactions, from photosynthesis to the combustion of its products, and plays an essential role in corrosion processes. The fast diffusion of hydrogen in most materials, including nonorganic matter such as oxides, makes hydrogen an omnipresent impurity [1]. Due to its polyvalent chemical character, hydrogen in matter may be present as a proton, as a neutral atom, or as an anion. As a consequence of its atomic number, hydrogen has only one electron. Particularly, this property is a challenge for many analytical tools based on the interaction with electrons: Core-level spectroscopies such as x-ray photoelectron spectroscopy (XPS) cannot be used as a quantitative method for hydrogen, because a photoemitted electron cannot be assigned to a hydrogen atom without any doubt, H^+ (e.g., OH) has formally no electrons, H^- has two, and in covalent bonds the H electron has a high probability density between the binding atoms; that is, the location of hydrogen electrons depends on the electronic structure of the material. The electronic structure, though, is the key to understanding the physical and chemical properties of matter, and photoemission spectroscopy is the standard experimental method to unravel it.

Obviously, materials in which the electronic structure is decisively influenced by hydrogen are particularly difficult to analyze. The archetypal example of this materials class is hydrogen-intercalated tungsten trioxide, H_xWO_3. Already in the nineteenth century, Berzelius noticed a color change when hydrogen gas was passed over tungsten trioxide [2]. Similar reversible optical and electrical changes are observed upon electrochemical insertion of alkali metals into WO_3 [3]. The discovery of the electrochromic properties of thin WO_3 films led to the development of a number of applications such as smart windows, displays, and variable mirrors [4,5]. As the above-discussed constraints for hydrogen do not apply here, the electronic structure of alkali-metal-intercalated tungsten bronzes, e.g., Na_xWO_3, are well characterized [6,7]. With the help of electronic structure modeling [8,9], there is consensus about the underlying physical phenomena of the chemical modification induced by alkali-metal intercalation [10]. In short, the electron of the alkali metal forms a new state in the band gap (conducting phase), but the phase initially remains insulating due to Coulomb interactions. In Na_xWO_3, a metal-insulator transition occurs at $x = 0.24$; similar behavior is found for the other alkali-metal-intercalated tungsten bronzes [9,11]. Although intuitively similar, the changes taking place during hydrogen intercalation are different and controversially debated. Simplified, there are two models: Hydrogen is intercalated into WO_3 and remains there, most likely as hydroxide; the corresponding electron affects the valence band in a similar way to the ones originating from alkali metals [8,12].

*andreas.borgschulte@empa.ch

The second model proposes that hydrogen can form water with oxygen from WO_3 and leave the now substoichiometric crystal [13]. The corresponding oxygen vacancies are filled with electrons. The loss of oxygen from the lattice induces distortions, leading to the localization of the electrons, that are described by an electron polaron model [14]. Summarizing, the origin of the controversy stems from the inability to detect and characterize hydrogen in the oxide.

In contrast to the electronic structure, the crystal structures of hydrogen and alkaline-metal-intercalated WO_3 are well studied. Most alkaline metal bronzes have a perovskite structure, where the alkaline metal occupies the central position [3]. The structure of hydrogen-intercalated WO_3 was determined by x-ray diffraction (XRD) and neutron diffraction on deuterium analogs [15,16]. It revealed a distorted cubic structure, where the hydrogen occupies a position 1.1 Å from the oxygen along the diagonal through the central position. This was supported by density functional theory (DFT) calculations on cubic WO_3 and HWO_3 finding the minimum energy position of hydrogen in the WO_3 lattice at a distance of 1.03 Å from the oxygen atoms [8]. Electronic structures have been calculated for hydrogen and alkali-metal intercalation explaining the observed changes at high intercalant concentration [8,17].

Experimentally, the intercalation process can be performed in two different ways. Electrochemical hydrogen insertion is relatively facile, but the electrochemical surface changes due to the aqueous environment hinder photoemission measurements. Gaseous hydrogen intercalation into WO_3 does not change the surface but is feasible only at UHV-incompatible pressures and in the presence of dissociatively active sites [18], limiting photoemission experiments to the study of *postmortem* samples.

In this paper, we present *in situ* photoemission data obtained by the membrane photoemission approach [19]: We employ a sample holder that enables varying the hydrogen pressure up to 1 bar while keeping the tungsten oxide thin film under UHV conditions necessary for photoelectron spectroscopy experiments [19] (see Fig. 1). This allows us to measure the pressure-composition isotherm of WO_3 by photoelectron spectroscopy. Synchrotron light enables probing of oxygen and tungsten core levels and the valence band states as a function of hydrogen content. The *operando* approach facilitates interpretation, as effects from unavoidable substoichiometries of the sample and other experimental uncertainties can be separated from the effects expected from hydrogen intercalation. Furthermore, we compare the photoemission results with DFT calculations, supporting the interpretation of experimental results in light of a polaron model.

II. EXPERIMENT

A. Sample preparation

WO_3 was deposited on palladium by electrodeposition from a H_2WO_4 solution. The H_2WO_4 solution was prepared in a round-bottom flask by suspending 0.92 g tungsten powder (99.9%; Sigma-Aldrich) in 7.5 ml water. The suspension was heated to 60 °C, and 3.5 ml H_2O_2 (30%; Merck) were
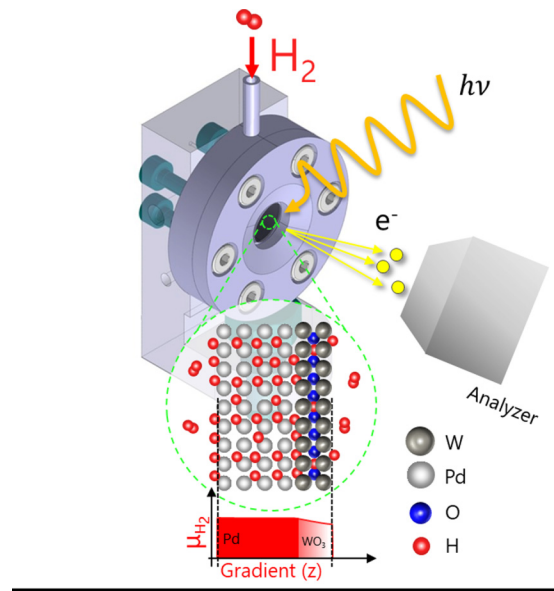

FIG. 1. Sketch of the membrane XPS sample holder and the experimental setup. The enlarged area shows the hydrogen permeation and the hydrogen chemical potential through the membrane. At steady state, the chemical potential on the feed side of the membrane is nearly equal to that on the vacuum side allowing the measurement of hydrogen concentrations in the material corresponding to atmospheric pressures by surface science techniques [19,20].

added. Tungsten was oxidized to tungstic acid accompanied by vigorous gas formation (H_2), and after 2 min a colorless, clear solution was obtained. A platinum wire was added to decompose the excess of H_2O_2 until no more oxygen bubbles evolved, which took 8 h at 60 °C. A final tungstic acid concentration of 50 mM was obtained by adding 50 ml of isopropyl alcohol and filling up with water to a total volume of 100 ml. Electrodeposition was performed in a two-electrode setup. A 2×2-cm foil of Pd with 47 μm thickness (purity 99.95%; Goodfellow) with its back side covered with Kapton tape served as working electrode, and a Pt wire served as counterelectrode. Since the WO_3 deposition on Pd competes with H_2 formation, relatively high current densities of approximately -2 mA/cm^2 were applied in chronopotentiometry mode for 10 min, which resulted in an amorphous blue film of approximately 30 nm thickness, as determined by XRD and energy dispersive x-ray (EDX) analysis, respectively. The sample was then dried in air on a hot plate at 200 °C for 10 min.

B. Membrane sample holder

The high-pressure XPS study reported here is based on the Pd membrane approach that we previously presented [20]. The photoelectron spectroscopy measurements were carried out at the GasPhase beamline of the Elettra synchrotron light source in Trieste, Italy. The beamline is equipped with a dedicated differential pumping system [21]. The combination of a high-resolution monochromator with the high transmission of the electron analyzer allowed us to collect spectra with a minimal energy resolution of 50 meV [22].

Briefly, the idea behind the embedded membrane approach is the following. The sample holder sketched in Fig. 1 consists of a hydrogen-permeable Pd membrane which is exposed on one side to high hydrogen pressure (up to 1 bar) and on the other side to UHV (10^{-8} mbar). Hydrogen is fluxed on the high-pressure side of the membrane, and following permeation, it reaches the surface exposed to vacuum in the form of atomic hydrogen. The tungsten oxide film, which is deposited on the analyzed side of the membrane, is thereby hydrogenated. Since the hydrogen permeation in the palladium membrane is much faster than in tungsten oxide, the oxide layer blocks hydrogen permeation. This creates a constant hydrogen concentration, and therefore a constant chemical potential, in the palladium membrane [19]. It is thereby possible to control the chemical potential of hydrogen on the UHV side of the membrane by the applied hydrogen pressure (see Fig. 1). The validity of the assumption of the equality of chemical potentials is experimentally evidenced by the permeation kinetics: The analysis gives surface-limited permeation (see Appendix, Fig. 9).

Photoemission measurements require this system to be in a pressure-temperature equilibrium state. In order to realize that, both the gas pressure and the membrane temperature were adjusted. The membrane was heated up to $160\,^{\circ}$C by means of a heating filament, and the hydrogen flux was controlled through a valve and a pressure gauge. Pressure-dependent spectra were obtained as follows. Hydrogen was constantly fluxed inside the sample holder; an equilibrium condition is reached when the amount of absorbed gas compensates the desorption process which occurs on the UHV side of the membrane [20]. When this steady state has been reached, the pressures on the two sides of the membrane are stable, and the measurement can be performed. The hydrogen amount inside the experimental chamber and hence the desorption process were monitored by means of a quadrupole residual gas analyzer (see Appendix, Fig. 9).

C. Photoelectron spectroscopy

In situ synchrotron measurements were recorded using 700 eV photon energy for the survey spectra and 104 eV for the simultaneous detection of tungsten $4f$ core levels and the valence band. During hydrogenation experiments, the photoemission spectra were recorded continuously in single-sweep mode, with each spectrum taking approximately 120 s. The applied hydrogen pressure was measured by an external pressure gauge. As soon as the partial hydrogen pressure in the chamber was constant, the external hydrogen pressure was increased. This led to approximately ten spectra being recorded for each external hydrogen pressure. These spectra were averaged for the subsequent data evaluation to improve signal-to-noise ratios. Data analysis was performed using the CASAXPS software, employing the GL(30) line shape, Shirley background subtraction, and a 2.1-eV spin orbit splitting for both W^{5+} and W^{6+} doublets [23]. The W $5p_{3/2}$ core level is not fitted in the spectra recorded at 104 eV, due to its small photoionization cross section at this photon energy [24]. The binding-energy calibration was performed on the gold-coated sample holder, setting the Au $4f_{7/2}$ peak to 84.0 eV. Due to small photon energy instabilities and work function changes

during hydrogenation, all spectra were subsequently aligned by shifting the W^{6+} $4f_{7/2}$ peak to 35.8 eV. These shifts are on the order of 0.2–0.3 eV.

Ex situ measurements were performed using a PHI Quantes spectrometer (ULVAC-PHI) equipped with a monochromatic Al Kα (1486.6 eV) x-ray source. Charge neutralization was accomplished by a dual-beam charge neutralization system, employing low-energy electron and argon ion beams. (Detailed acquisition parameters are given in the Appendix, Table I.)

D. Electronic structure calculation

Calculation of electronic structure by density functional theory (DFT) and hybrid DFT was performed using the Vienna *ab initio* simulation package (VASP) [25–28]. The calculation used the projector augmented-wave (PAW) method [29,30] to describe the effects of core electrons, and Perdew-Burke-Ernzerhof (PBE) [31] implementation of the generalized gradient approximation (GGA) for the exchange-correlation functional. The energy cutoff was 600 eV for the plane-wave basis of the valence electrons. The electronic structure was calculated on a $15 \times 15 \times 15$ Γ-centered mesh for WO_3 (unit cell), and a $4 \times 4 \times 4$ Γ-centered mesh for H_xWO_3 ($2 \times 2 \times 2$ supercell). The total energy tolerance for electronic energy minimization was 10^{-6} eV, and for structure optimization it was 10^{-5} eV. The maximum interatomic force after relaxation was below 0.01 eV/Å. After structural optimization, hybrid-DFT calculation of the band structure was performed using the Heyd-Scuseria-Ernzerhof HSE06 hybrid functional [32,33] with a mixing parameter of 25% and a screening parameter of 0.2 AA^{-1}.

Hydrogen-free WO_3 crystallizes in the monoclinic structure with space group $P2_1/n$ with $a = 7.304$ Å, $b = 7.536$ Å, $c = 7.691$ Å, and $\beta = 90.85°$ [34]. Other polymorphs exist depending on temperature [35]. However, intercalation of hydrogen leads to the formation of cubic structures of H_xWO_3 for $x = 0.5$ [16]. We thus simplified the calculations using the cubic ReO_3 structure where the metal is surrounded by six oxygen atoms in an octahedron (see Fig. 2) for all compositions including hydrogen-free WO_3. With this constraint, the calculated electronic structure is that of an artificial structure with slight deviations from reality. A simple quality parameter is the optical gap [17,36]. The calculated direct band gap of simple cubic WO_3 with around 2.3 eV matches the experimental values of 2.6–3.3 eV for the direct band gap [13,36,37]. This difference is due to the general underestimation of the optical gap by GGA and weighted density approximation (WDA) methods [38], with WO_3 being particularly notorious [39]. Furthermore, calculations of the gap of the simple cubic phase yield smaller gaps than the ones calculated for the monoclinic phase of bulk tungsten trioxide [8,17,40]. Values vary from 0.69 eV [revised PBE (RPBE)] and 2.25 eV (PBE8) for the simple cubic system to 1.3 eV (RPBE) and 3.68 eV (PBE8) for the monoclinic system, with the functional indicated in brackets [39]. However, the simplicity of a cubic system allows the modeling of the partially hydrogenated bronzes H_xWO_3 with $x = 0$, 0.25, 0.75, and 1.0. For $x = 0.25$, two hydrogens with antiparallel spin configuration are placed in a simple cubic eightfold unit

TABLE I. Acquisition parameters for XPS and synchrotron photoelectron spectroscopy.

	Energy range (eV)	Pass energy (eV)	Energy step size (meV)	Total acquisition time per point (s)
Ex situ XPS survey	1100–0	112	100	0.4
Ex situ XPS narrow scan	variable	55	50	1.2
In situ XPS survey	550–0	20	200	0.6
In situ XPS narrow scan	variable	20	50	0.1

cell of WO_3 (see Fig. 2 and the Appendix, Fig. 10). Nine different hydrogen constellations were calculated, with the two hydrogen atoms placed in the unit cells along the 100, 110, and 111 directions, respectively. The difference between these constellations turned out to be negligible (Appendix, Fig. 10). The hydrogen and oxygen positions were released in the subunit to find the H-O position with minimum total energy. We found an optimum for $d_{O\text{-}H} = 1.03$ Å, in good agreement with the literature [8]. In addition, the oxygen tetrahedrons were distorted (Fig. 2). Similar calculations were performed for $H_{0.75}WO_3$ using six hydrogens per eightfold unit cell. For better comparison, the calculated total density of electron states is broadened by 0.5 eV to match the experimental resolution of photoemission spectroscopy (see Fig. 5).

III. RESULTS

For characterization, XPS measurements employing Al Kα radiation were performed on the tungsten-oxide-coated palladium membrane pre- and posthydrogenation (see Appendix, Fig. 7). The results are in perfect agreement with the literature; that is, we find mainly W^{6+} and some W^{5+} as extracted by peak fitting of the W $4f$ states [41], which is typical for amorphous WO_3 thin films [42]. There is no significant difference between the data taken *ex situ* before and after hydrogen exposure. The survey spectra show less carbon contamination and the presence of Pd $3d$ peaks after hydrogenation, the latter are attributed to inadvertent removal of the thin WO_3 layer
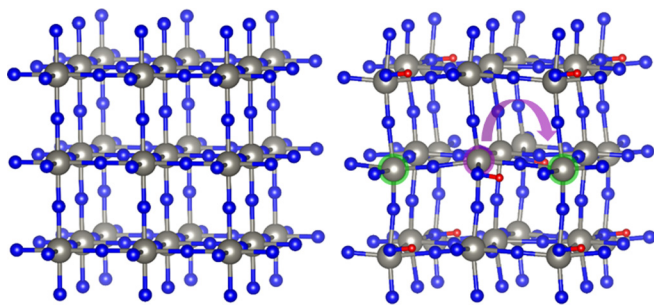
during mounting or dismounting from the membrane sample holder.

The same procedure was applied *in situ* directly before and after hydrogen exposure (Appendix, Fig. 8). After hydrogen exposure the ratio W^{5+}/W^{6+} increases. The intensity of the higher-binding-energy shoulder of the O $1s$ peak, indicative of OH and/or carbonate species [42], increases in parallel (Appendix, Fig. 8). These changes were followed *in situ* at various hydrogen pressures applied to the membrane. We observed continuous variations of core levels (Fig. 3) as well as the valence band [Fig. 5(b)] indicative of hydrogen intercalation into WO_3. However, in addition to the effects assigned to hydrogen exposure, we found a higher W^{5+}/W^{6+} ratio derived from *in situ* measurements at 700 eV than the one derived *ex situ* at 1486.6 eV photon energy, both measured on the sample before hydrogen exposure. This effect is attributed to the prolonged UHV exposure necessary to align the experimental setup. During alignment and optimization of the acquisition parameters, the membrane was exposed to UV radiation of 104 eV photon energy. It is well known that UV radiation induces the reduction of WO_3, leading to larger fractions of W^{5+} [43]. This effect is a major detriment of photoelectron spectroscopy applied to such systems in general.

The *in situ* hydrogenation opens the possibility to disentangle the effects from radiation damage and hydrogen exposure by following the evolution of the spectra with and without hydrogen. In Fig. 3, the WO_3 thin film was exposed to

FIG. 2. Illustration of the cubic crystal structure of WO_3 (left) and of one polymorph of $H_{0.25}WO_3$ (right) as used for modeling. Note the distortion of the oxygen atoms (blue) induced by hydrogen (red) amounts as little as $x = 0.25$. This distortion is local: As an example, two tungsten atoms (gray) exclusively surrounded by oxygen atoms are highlighted with a green corona, and one tungsten atom surrounded by five oxygens and one OH group is highlighted with a purple corona. In the local picture, the latter atoms are W^{5+}, and the ones surrounded solely by oxygen are W^{6+}. Moving an electron and hydrogen (arrow) requires structural rearrangements.
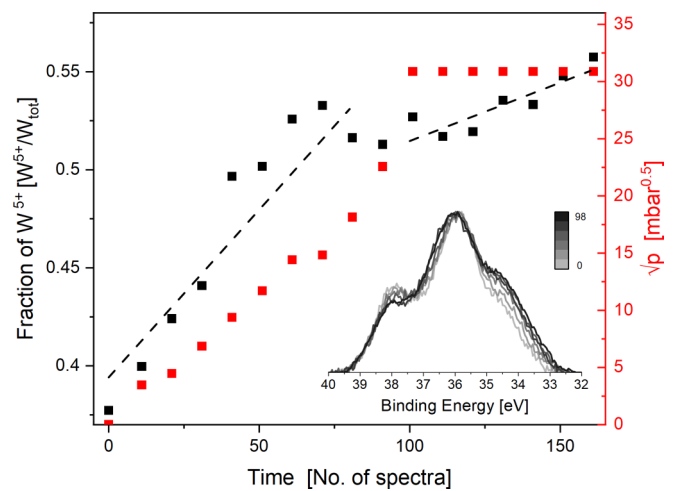

FIG. 3. The fraction of W^{5+} in the sample, as derived from peak fitting shown in the Appendix (Fig. 7), is shown in black, with the linear interpolation of the slope shown by the dashed gray lines during the increasing hydrogen pressure and the constant hydrogen pressure phases, shown in red. The grayscale spectra show the changes in the W $4f$ spectra during the increasing hydrogen pressure phase.
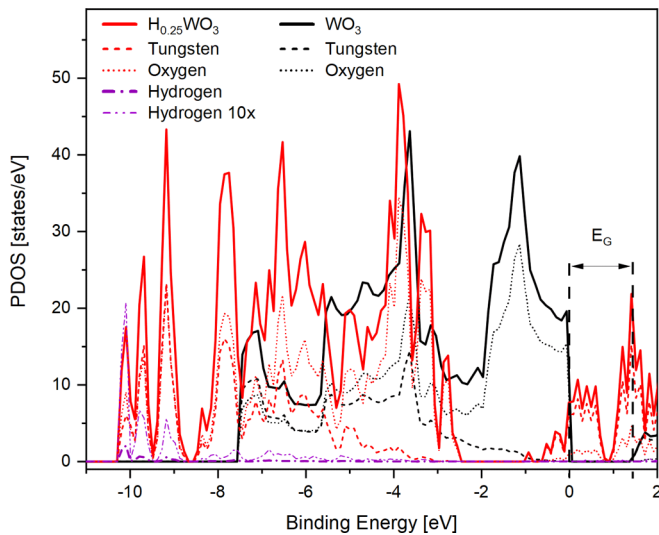
FIG. 4. Modeled partial DOS (PDOS) and total DOS of cubic WO_3 (black line) and H_xWO_3 (red line) with hydrogen concentrations as small as $x = 0.25$. $E_G = 1.3$ eV is the indirect band gap in WO_3 derived from the onsets of valence and conduction bands. Full band structure calculations give the direct band gap of 2.3 eV (not shown). Note the minimal contribution of hydrogen electrons (purple dash-dotted line) to the total density of states in $H_{0.25}WO_3$.

increasing hydrogen back pressure up to 1 bar and then kept under these conditions for a long period. The increase in the W^{5+} fraction shows two different slopes. With increasing the hydrogen back pressure, the amount of W^{5+} grows fast. When the hydrogen back pressure is high but constant, the growth of W^{5+} slows down markedly. The amount of W^{5+} purely from hydrogenation may then be the difference between the two dashed fitting curves, neglecting a mutual enhancement of the two effects. The hydrogen content in H_xWO_3 has been shown to be proportional to the square root of the applied hydrogen pressure [18,44]. With this relation, the amount of W^{5+} is proportional to $\sqrt{p_{H_2}}$ and thus to the amount of hydrogen x in $H_xWO_{3-\delta}$. An uncertainty is the number of oxygen vacancies δ. The measured differences in the O-to-W elemental ratio between pre- and posthydrogenation are less than 3% (Appendix, Fig. 8). This lies within the accuracy of the measurements. Within this limitation, there is no oxygen loss during hydrogenation.

The measurement of valence band spectra was performed in parallel to the W $4f$ core levels, showing subtle changes with hydrogenation as well (Fig. 6). However, in contrast to the binding-energy shifts of core levels, which can be interpreted rather easily [45,46], the H $1s$ state is both core level as well as valence state, and thus not easily characterized. This challenge is tackled by an in-depth analysis of the valence band spectra with the help of DFT calculations.

DFT calculations were performed on simple cubic WO_3, $H_{0.25}WO_3$, $H_{0.75}WO_3$, and H_1WO_3 to illustrate the effects of hydrogenation on the electronic structure. WO_3 exhibits typical features of a semiconductor with a direct band gap of about 2.3 eV and an indirect one of 1.3 eV as derived from band structure calculations (see Fig. 4). As discussed in Sec. II D, the gap is underestimated (the experimental gap of monoclinic
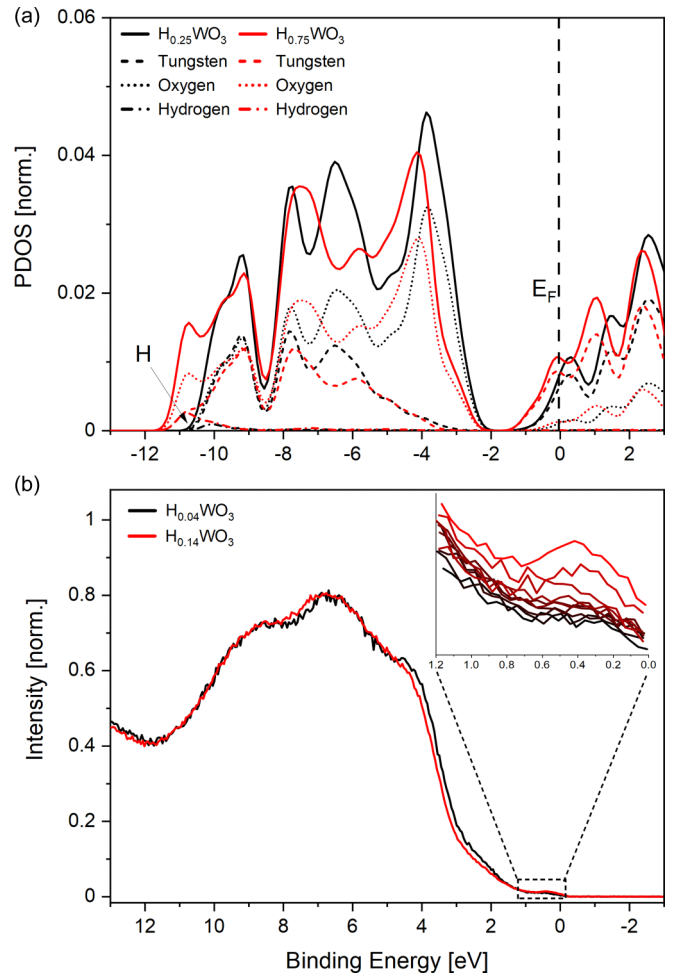

FIG. 5. (a) Calculated partial and total DOS of $H_{0.25}WO_3$ (black) and $H_{0.75}WO_3$ (red). (b) Measured photoemission spectra of minimum and maximum hydrogen content in black and red. The hydrogen contents as labeled are derived from the peak intensities of the peak evolving with hydrogen pressure as shown in the inset (see Fig. 6 and text for more information).

WO_3 is 3.2 eV [13,37]) due to the assumption of a cubic lattice, which simplifies the calculation of hydrogen-intercalated WO_3. Nevertheless, the overall electronic structure with the valence band edge dominated by oxygen orbitals is in perfect agreement with the literature. This is also in agreement with experimental observations: The optical absorption in crystalline H_xWO_3 is very similar to that in amorphous H_xWO_3 indicating that the crystallinity plays only a minor role in electronic structure changes upon hydrogenation [47].

The intercalation of hydrogen into WO_3 was modeled by placing hydrogen in the center of the WO_3 subunit and optimizing its position in the simple cubic structure by energy minimization. The minimum was found with hydrogen occupying a position near one oxygen site with a distance of 1.04 Å identical to the calculations of Hjelm *et al.* [8], and very similar to the bond length of an OH ion. Simultaneously, the lattice is slightly distorted (Fig. 2). The presence of hydrogen accompanied by the lattice distortion leads to two main changes in the electronic structure (see Fig. 4): The valence band broadens due to the bonding of oxygen with hydrogen
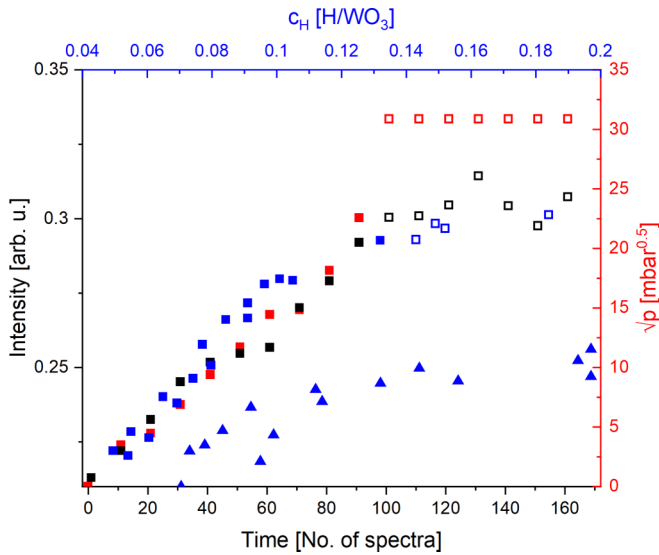
FIG. 6. The intensity of hydrogen-induced, conduction-band-like tungsten states (black) are shown as a function of time and with hydrogen back pressure (red). Solid symbols indicate increasing hydrogen pressure, and open ones mean constant hydrogen back pressure. The bulk pressure-composition isotherm data on Pt:WO$_3$ (blue) at 423 K are plotted on the same pressure axis [18]. Squares represent absorption data, whereas triangles represent desorption data.

(bonding states around -11 eV), and the conduction band minimum dominated by tungsten states is being occupied by electrons donated by the hydrogen and pushed below the Fermi level. It is expected that these changes lead to large increases in the electronic conductivity, which will be discussed in Sec. IV. However, the aim of this paper is to confirm these effects by photoelectron spectroscopy, as these states should be observable.

Figure 5 shows the calculated density of states (DOS) for H$_{0.25}$WO$_3$ and H$_{0.75}$WO$_3$ that have been broadened to account for the natural linewidth of the photoemission process and valence band spectra at low and high applied hydrogen back pressure. The effects of going from H$_{0.25}$WO$_3$ to H$_{0.75}$WO$_3$ (see Fig. 5) are less drastic compared with the difference between WO$_3$ and H$_x$WO$_3$ (see Fig. 4). Most striking are the increasing hydrogen-oxygen bonding states and corresponding broadening of the oxygen states, which leads to a decrease in the DOS near 3 eV binding energy. The second effect, most relevant to this paper, is the increase in tungsten states near E_F with increasing hydrogen content. These two changes match the experimental spectra exceptionally well (Fig. 5). In particular, the calculations confirm the existence of hydrogen-induced states near E_F, which are associated with tungsten states.

The normalized peak area of these hydrogen-induced tungsten states at 0.4 eV binding energy scales with the square root of the hydrogen back pressure (Fig. 6). It is important to note that it does not evolve any further with time at constant pressure, which excludes its origin induced by radiation damage and confirms that the measured state is in thermodynamic equilibrium with hydrogen gas. Since the number of hydrogen-induced tungsten states is directly re-

lated to the applied hydrogen back pressure by employing our membrane approach, we plot it together with the bulk pressure-composition isotherm of Pt:WO$_3$ reported in the literature [18] using the common pressure axis. Using this calibration, we extract that the initial hydrogen content in our thin films is H$_{0.04}$WO$_3$ increasing to H$_{0.14}$WO$_3$ at 1000 mbar.

IV. DISCUSSION

Already in the past, Hollinger *et al.* proposed that coloration in amorphous tungsten oxide films upon hydrogenation is connected to an increase in localized electronic states (W^{5+}), but they could not disentangle whether the origin of the effect was from oxygen defects caused by UV exposure or from hydrogen intercalation [48]. The optical absorption band corresponds to a peak near the Fermi level detected by photoelectron spectroscopy.

With this, our measurements confirm most of the literature data on electronic structure changes in H$_x$WO$_3$ or substoichiometric WO$_{3-\delta}$, in particular, the evolution of the peak near the Fermi level [14,23,41,43,48]. However, with our experimental procedure we can disentangle the contributions from oxygen deficiency and hydrogen incorporation. The membrane photoemission measurements show that hydrogen interaction with WO$_3$ leads to band-gap states without the loss of oxygen (Appendix, Fig. 8).

Attributing these states near the Fermi level to hydrogen is too short viewed. Even without sophisticated band structure calculations we can estimate the potential effect: The valence band of H$_x$WO$_3$ consists of 3×6 O $2p$ states (we neglect here the small contribution of W $5d$) and at most 0.2 hydrogens. In addition, we have to consider the photoionization cross section of electrons localized on hydrogen and oxygen of 0.02 and 1 Mb, respectively, at around 104 eV [24]. The expected intensity ratio between hydrogen states and total valence states is $0.2/(3 \times 6) \times 0.02/1 = 2.2 \times 10^{-4}$. It is thus unlikely that the photoelectrons near E_F stem from hydrogen. Instead, the DFT modeling shows that hydrogenation of WO$_3$ leads to the formation of OH with hydrogen states appearing at -11 eV and tungstenlike conduction band states near the Fermi level (Fig. 5).

Conductivity and optical experiments evidence that hydrogen-intercalated WO$_3$ is not an electronic conductor at small hydrogen content in contrast to what is suggested by the calculated DOS (Fig. 4), which shows states at E_F. This discrepancy was already found in the past and explained by correlation models [49]. In the local picture, hydrogen intercalation gives

$$\text{W}^{6+}\text{O}_3^{2-} \xrightarrow{\text{H}} \text{W}^{5+}(\text{OH})^-\text{O}_2^{2-}, \tag{1}$$
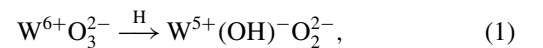
with the electron from the hydrogen localized by the OH bond. With this, the nearby tungsten atom is different from the ones surrounded solely by oxygen atoms (Fig. 2). This local picture is still compatible with the band structure; however, dynamic properties depend on the correlation of the corresponding electrons. Such calculations are beyond the scope of this paper. We restrict ourselves to the following simplified picture explaining the observation that despite having electrons near the Fermi level (Fig. 5), H$_x$WO$_3$ does not exhibit metallic character (no Drude absorption [13]): The movement

of electrons associated with the tungsten atom near the OH group (W^{5+}) is correlated with the hopping of the proton, which requires crystallographic rearrangement as the oxygen orientations around the tungsten atoms are slightly different (see Fig. 2).

Crandall and Faughnan [49] find a metal-insulator transition around hydrogen concentrations of approximately 0.3, which is close to that predicted by percolation theory. At the percolation threshold, the hopping between the tungsten atoms will form a continuous chain throughout the crystal. Further evidence for the localization of these electrons was provided by optical absorption spectroscopy where amorphous H_xWO_3 exhibits an absorption maximum in the near-infrared range [4,50]. The optically induced jumping of the electron from one W site (W_a) to the other (W_b) is a special charge-transfer excitation, which is well described by the so-called polaron model [13]:

$$W_a^{5+}(OH) + W_b^{6+}O \xrightarrow{\hbar\omega} W_a^{6+}O + W_b^{5+}(OH). \quad (2)$$
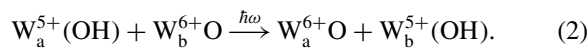
In contrast to Saenger *et al.* [13], who attribute the corresponding interaction of this electron to the surrounding distorted oxygen-deficient lattice, we propose the interaction to be between the proton and the electron on W^{5+} also leading to a distorted lattice. This so-called proton polaron has been proposed for describing the proton transport in a similar system, hydrated $BaCe_{0.8}Y_{0.2}O_{3-\delta}$ [51]. The general underlying principle, the required crystalline rearrangements linked to charge transfer ("movement of distortions," Fig. 2; and energy dependence on hydrogen constellation, Appendix, Fig. 10), remains the same. The metal oxygen rearrangement proceeds through vibrations of the WO_6 octahedra and O-H vibrations. The mobility of protons may thus be in both cases a result of phonon-assisted jumps. The changes in the electronic structure by a proton-oxygen bond also explain the difference from changes induced by oxygen vacancies. Here, recent DFT calculations provide arguments that oxygen vacancies in WO_3 introduce "free" carriers to the conduction band, because the corresponding electrons are delocalized over a large area [52]. In our case, the OH bond pins a similar electron brought into the system by hydrogen intercalation. From an electron spectroscopy point of view, this difference is indistinguishable, but the localized picture is in good agreement with other physical properties of $H_xWO_{3-\delta}$ (see discussion above).

Finally, tackling the difficulties of probing the electronic structure in $H_xWO_{3-\delta}$ by static electron spectroscopy by following dynamic changes *in situ* may be extended to ultrafast spectroscopy. With this, the degree of localization is directly accessible.

The main outcome of this study is the change in the electronic structure near the Fermi edge from oxygen-dominated orbitals to tungsten-dominated orbitals (see Fig. 4). This has drastic consequences for (electro)catalysis of oxygen-related reactions in addition to physical properties such as electron conductivity and optical properties as discussed above. WO_3 is one of the oxides considered to be a suitable photoelectrochemical water-splitting catalyst [53]. In particular, it shows a high activity for water oxidation in the presence of a suitable electron acceptor [53,54]. Hydrogen treatment of WO_3 can increase photocurrent significantly [54,55], which was

interpreted as an increase in the number of oxygen vacancies, and thus defect states. With our findings, we cannot exclude the existence of oxygen defect states in parallel with proton polarons. However, the more pronounced effect of hydrogen treatment compared with vacuum annealing [54,55] suggests that generally, hydrogen-related states are the main origin of the effect.

Similarly, the hydrogen-induced electronic structure near the Fermi edge explains the rather small effect on superconductivity in tungsten oxides, if compared with metal doping [56,57]. If hydrogen vibrations with H PDOS at E_F contributed to the superconductivity, a strong positive effect may be expected. However, the superconductivity in bulk WO_3 is currently understood to originate from a weak-coupling
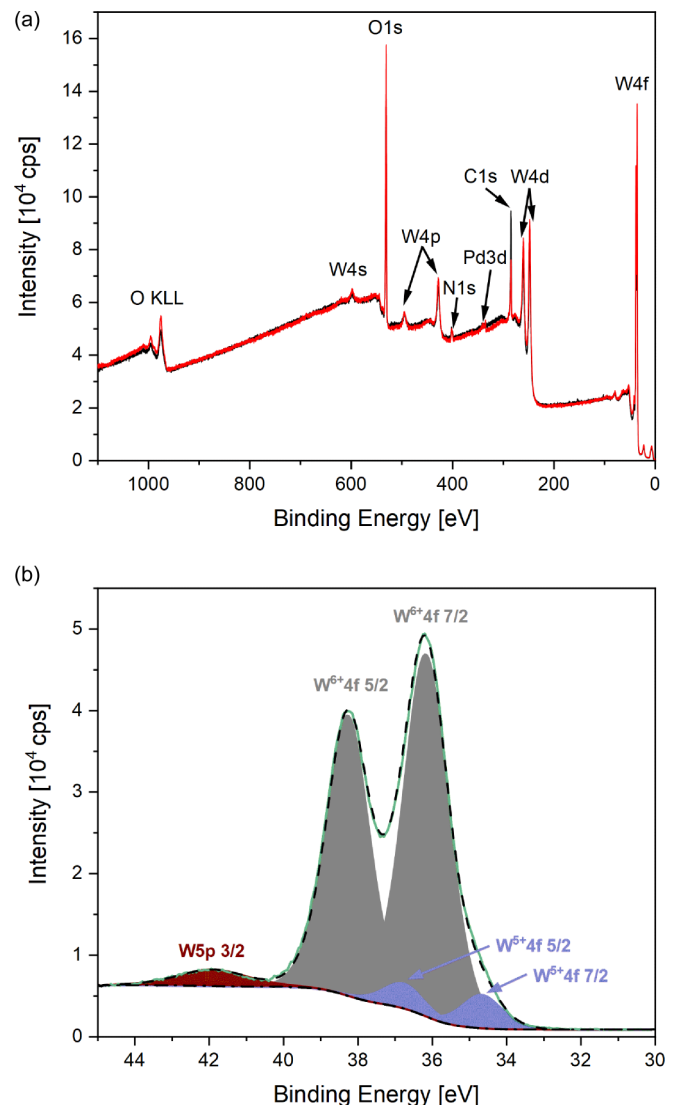

FIG. 7. (a) The pre- and posthydrogenation XPS survey spectra are shown in black and red, respectively. (b) The W $5p_{3/2}$ (brown) and W $4f$ (gray and violet) core levels of the electrodeposited WO_3 as prepared, as described in Sec. II A, measured by Al $K\alpha$ XPS. The spectra are fitted with two pairs of doublets giving the W^{6+} and W^{5+} fractions, respectively. The peak fitting indicates the sample being almost completely oxidized, with a small fraction of W^{5+} states present ($\simeq 7.7\%$).

state sustained by soft vibrational modes of the WO_6 octahedra [57], and the formation of OH instead of the creation of oxygen vacancies upon hydrogenation is in line with this argumentation.

V. CONCLUSIONS

We measured the palladium-assisted hydrogenation of tungsten trioxide by *operando* membrane XPS at hydrogen pressures up to 1 bar. The combination of the membrane XPS with synchrotron radiation allows us to measure both core levels and the valence band simultaneously up to high hydrogen pressures minimizing the effect of initial preparation parameters, beam damage, and exposure to the reducing UHV environment that would occur with consecutive XPS or ultraviolet photoelectron spectroscopy (UPS) measurements. Analysis of the tungsten $4f$ core levels shows an increase in W^{5+} with increasing hydrogen pressure. At the same time a state appears

close to the Fermi level that is connected to the hydrogen content in the compound. Although induced by hydrogen, the corresponding electrons are allocated to tungsten d states. Using previous reference measurements, it is possible to create a pressure-composition isotherm from the spectroscopy data. The photoemission measurements together with DFT calculations corroborate that the coloration of the films by hydrogen can be explained by a proton polaron model.

APPENDIX

1. Experimental details of the photoemission experiments

Table I shows the acquisition parameters used for XPS and synchrotron photoelectron spectroscopy.

Figures 7 and 8 compare the survey and W $4f$ core-level spectra as measured *ex situ* (XPS) and *in situ* (synchrotron photoemission) before and after hydrogenation. In addition, the deconvolution of the spectra to derive the W^{6+} and W^{5+} fractions is shown for one archetypal example. From the intensity ratio of O $1s$ to W $4f$, one can estimate that the oxygen loss is below 3%.

The rate-limiting step of the permeation of hydrogen through the membrane can be derived from the pressure dependence on both sides of the membrane:

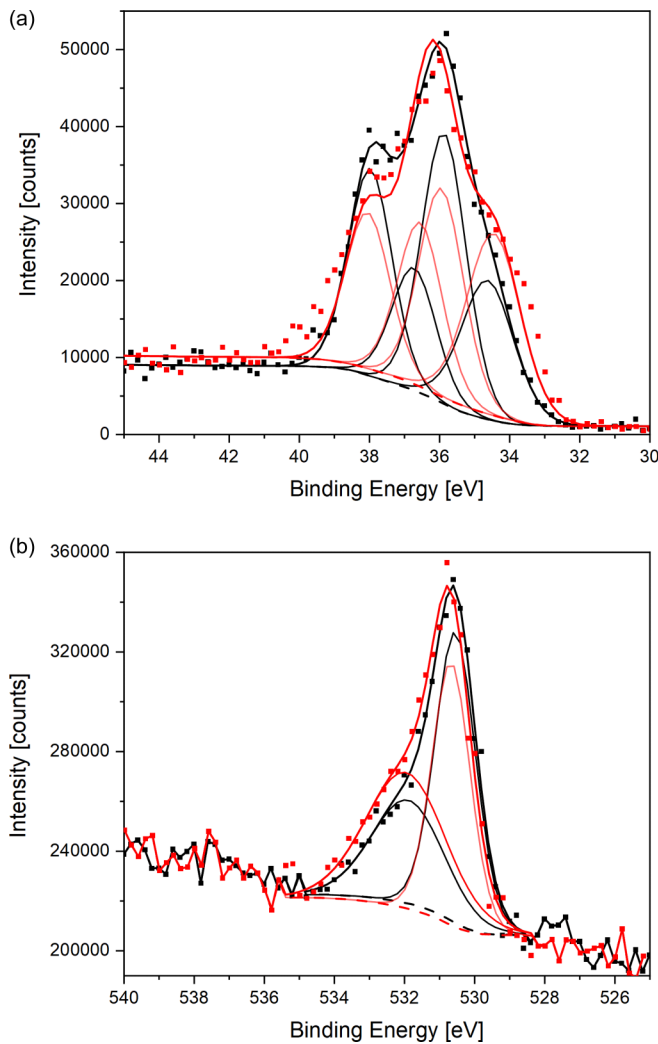$$p_{UHV} \propto p_{appl}^r. \tag{A1}$$

FIG. 8. W $4f$ (a) and O $1s$ (b) core-level spectra recorded using 700 eV photon energy. The spectra were recorded *in situ* before and after exposure to hydrogen (black and red, respectively). The W^{5+} fraction increases from 37.6 to 51.2% and the oxygen defect fraction from 38.8 to 52.0% upon hydrogenation. The intensity ratio of W to O remains nearly constant with $I(O_{latt})/I(W) = 1.06 \rightarrow 1.03$.
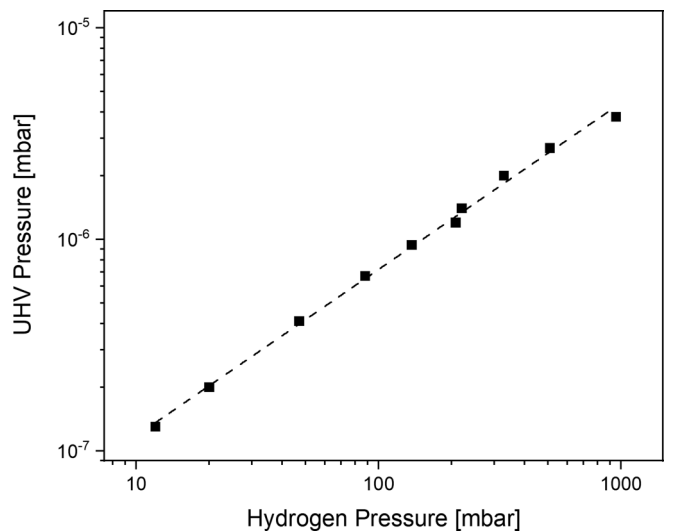

FIG. 9. Double-log plot of the measured hydrogen pressure in the vacuum chamber as a function of the applied feed pressure. A fit yields a slope of 0.79.
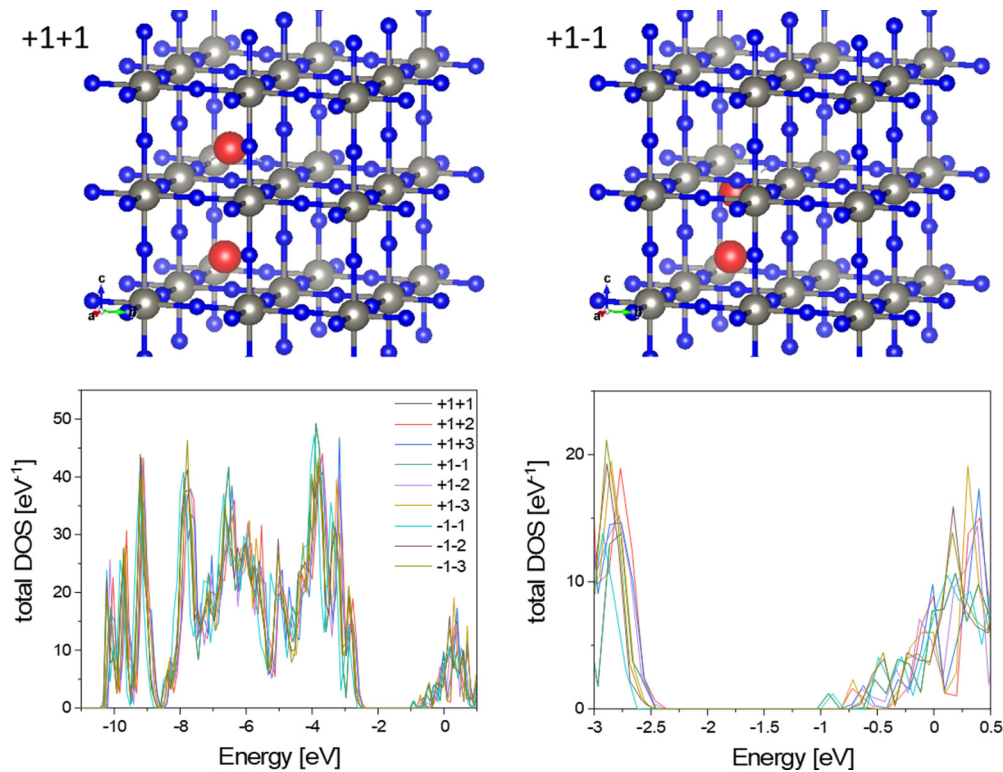
FIG. 10. Top: As an example, two different hydrogen constellations in $H_{0.25}WO_3$, denoted as $+1+1$ and $+1-1$, before relaxation. Bottom: DFT of nine different constellations. The right graph is an enlargement around the band gap.

For ideal cases, surface-limited permeation gives an exponent $r = 1$, and bulk diffusion gives $r = \frac{1}{2}$ [19,20]. A fit to the double-log plot of the measured hydrogen pressure in the vacuum chamber as a function of the applied feed pressure yields an exponent of 0.79 (Fig. 9), indicative of surface-limited kinetics.

2. Hydrogen constellations used for DFT calculations

Substoichiometric concentrations ($x < 1$) in H_xWO_3 are difficult to model. For $x = 0.25$, the unit cell of $H_{0.25}WO_3$ is extended to a $2 \times 2 \times 2$ supercell of the simple unit cell of H_1WO_3 based on one H in the WO_3 cell (Fig. 10). Not all of the now possible H positions are occupied to reflect the substoichiometry giving additional freedom as to where to place these hydrogen atoms relative to each other. We modeled nine archetypal constellations, where the hydrogen atoms are placed in the subcells along the 100, 110, and 111 directions and with different spin constellations. The corresponding energy shifts are of the order of 0.3 eV. This difference is neglected within the interpretation of the photoelectron spectra; however, the nonzero energy difference will contribute to the energy barrier for hydrogen motion in H_xWO_3.

[1] J. Völkl and H. Wipf, Diffusion of hydrogen in metals, Hyperfine Interact. **8**, 631 (1981).

[2] F. Wöhler, Ueber das Wolfram, Ann. Phys. (Berlin) **78**, 345 (1824).

[3] E. O. Brimm, J. C. Brantley, J. H. Lorenz, and M. H. Jellinek, Sodium and potassium tungsten bronzes, J. Am. Chem. Soc. **73**, 5427 (1951).

[4] S. K. Deb, Optical and photoelectric properties and colour centres in thin films of tungsten oxide, Philos. Mag. **27**, 801 (1973).

[5] C. G. Granqvist, Electrochromic tungsten oxide films: Review of progress 1993–1998, Sol. Energy Mater. Sol. Cells **60**, 201 (2000).

[6] H. Höchst, R. Bringans, H. Shanks, and P. Steiner, Failure of the rigid band model in Na_xWO_3: An XPS study, Solid State Commun. **37**, 41 (1981).

[7] S. Raj, T. Sato, S. Souma, T. Takahashi, D. D. Sarma, and P. Mahadevan, Metal-insulator transition of Na_xWO_3 studied by angle-resolved photoemission spectroscopy, Mod. Phys. Lett. B **23**, 2819 (2009).

[8] A. Hjelm, C. G. Granqvist, and J. M. Wills, Electronic structure and optical properties of WO_3, $LiWO_3$, $NaWO_3$, and HWO_3, Phys. Rev. B **54**, 2436 (1996).

[9] A. L. Larsson, B. E. Sernelius, and G. A. Niklasson, Optical absorption of Li-intercalated polycrystalline tungsten oxide films: Comparison to large polaron theory, Solid State Ionics **165**, 35 (2003).

[10] C. G. Granqvist, Bulk crystalline tungsten oxide, in *Handbook of Inorganic Electrochromic Materials* (Elsevier, New York, 1995), Chap. 2, p. 633.

[11] H. Höchst, R. D. Bringans, and H. R. Shanks, Electronic structure of Na_xWO_3: A photoemission study covering the entire concentration range, Phys. Rev. B **26**, 1702 (1982).

[12] X. Leng, J. Pereiro, J. Strle, G. Dubuis, A. T. Bollinger, A. Gozar, J. Wu, N. Litombe, C. Panagopoulos, D. Pavuna, and I. Božović, Insulator to metal transition in WO_3 induced by electrolyte gating, npj Quantum Mater. **2**, 35 (2017).

[13] M. F. Saenger, T. Höing, B. W. Robertson, R. B. Billa, T. Hofmann, E. Schubert, and M. Schubert, Polaron and phonon properties in proton intercalated amorphous tungsten oxide thin films, Phys. Rev. B **78**, 245205 (2008).

[14] M. B. Johansson, P. T. Kristiansen, L. Duda, G. A. Niklasson, and L. Österlund, Band gap states in nanocrystalline WO_3 thin films studied by soft x-ray spectroscopy and optical spectrophotometry, J. Phys.: Condens. Matter **28**, 475802 (2016).

[15] P. G. Dickens and R. J. Hurditch, X-ray and neutron diffraction studies of a tetragonal hydrogen bronze H_xWO_3, Nature (London) **215**, 1266 (1967).

[16] P. Wiseman and P. Dickens, The crystal structure of cubic hydrogen tungsten bronze, J. Solid State Chem. **6**, 374 (1973).

[17] G. A. de Wijs and R. A. de Groot, Structure and electronic properties of amorphous WO_3, Phys. Rev. B **60**, 16463 (1999).

[18] A. R. Berzins and P. A. Sermon, Reversible isothermal sorption of hydrogen by tungsten trioxide in presence of platinum, Nature (London) **303**, 506 (1983).

[19] R. Delmelle, B. Probst, R. Alberto, A. Züttel, D. Bleiner, and A. Borgschulte, Closing the pressure gap in x-ray photoelectron spectroscopy by membrane hydrogenation, Rev. Sci. Instrum. **86**, 053104 (2015).

[20] O. Sambalova and A. Borgschulte, Membrane concept for environmental surface science, J. Alloys Compd. **742**, 518 (2018).

[21] R. Blyth, R. Delaunay, M. Zitnik, J. Krempasky, R. Krempaska, J. Slezak, K. Prince, R. Richter, M. Vondracek, R. Camilloni, L. Avaldi, M. Coreno, G. Stefani, C. Furlani, M. de Simone, S. Stranges, and M.-Y. Adam, The high resolution gas phase photoemission beamline, Elettra, J. Electron Spectrosc. Relat. Phenom. **101-103**, 959 (1999).

[22] C. Grazioli, Photoionization experiments in the study of energy transfer in nanostructured materials and their precursors, Ph.D. thesis, Università degli Studi di Trieste, 2017.

[23] O. Bouvard, A. Krammer, and A. Schüler, *In situ* core-level and valence-band photoelectron spectroscopy of reactively sputtered tungsten oxide films, Surf. Interface Anal. **48**, 660 (2016).

[24] J. J. Yeh and I. Lindau, Atomic subshell photoionization cross sections and asymmetry parameter: $1 < Z < 103$, At. Data Nucl. Data Tables **32**, 1 (1985).

[25] G. Kresse and J. Hafner, *Ab initio* molecular dynamics for liquid metals, Phys. Rev. B **47**, 558 (1993).

[26] G. Kresse and J. Hafner, *Ab initio* molecular-dynamics simulation of the liquid-metal-amorphous-semiconductor transition in germanium, Phys. Rev. B **49**, 14251 (1994).

[27] G. Kresse and J. Furthmüller, Efficiency of ab-initio total energy calculations for metals and semiconductors using a plane-wave basis set, Comput. Mater. Sci. **6**, 15 (1996).

[28] G. Kresse and J. Furthmüller, Efficient iterative schemes for *ab initio* total-energy calculations using a plane-wave basis set, Phys. Rev. B **54**, 11169 (1996).

[29] P. E. Blochl, Projector augmented-wave method, Phys. Rev. B **50**, 17953 (1994).

[30] G. Kresse and D. Joubert, From ultrasoft pseudopotentials to the projector augmented-wave method, Phys. Rev. B **59**, 1758 (1999).

[31] J. P. Perdew, K. Burke, and M. Ernzerhof, Generalized Gradient Approximation Made Simple, Phys. Rev. Lett. **77**, 3865 (1996).

[32] J. Heyd, G. E. Scuseria, and M. Ernzerhof, Hybrid functionals based on a screened Coulomb potential, J. Chem. Phys. **118**, 8207 (2003).

[33] A. V. Krukau, O. A. Vydrov, A. F. Izmaylov, and G. E. Scuseria, Influence of the exchange screening parameter on the performance of screened hybrid functionals, J. Chem. Phys. **125**, 224106 (2006).

[34] E. Lassner and W.-D. Schubert, *Tungsten Properties, Chemistry, Technology of the Element, Alloys, and Chemical Compounds*, 1st ed. (Springer, New York, 1999).

[35] H. A. Wriedt, The O-W (oxygen-tungsten) system, Bull. Alloy Phase Diagrams **10**, 368 (1989).

[36] P. P. González-Borrero, F. Sato, A. N. Medina, M. L. Baesso, A. C. Bento, G. Baldissera, C. Persson, G. A. Niklasson, C. G. Granqvist, and A. Ferreira da Silva, Optical band-gap determination of nanostructured WO_3 film, Appl. Phys. Lett. **96**, 061909 (2010).

[37] M. Green and Z. Hussain, Optical properties of dilute hydrogen tungsten bronze thin films, J. Appl. Phys. (Melville, NY) **69**, 7788 (1991).

[38] K. Xiong, J. Robertson, and S. J. Clark, Behavior of hydrogen in wide band gap oxides, J. Appl. Phys. (Melville, NY) **102**, 083710 (2007).

[39] F. Wang, C. Di Valentin, and G. Pacchioni, Electronic and structural properties of WO_3: A systematic hybrid DFT study, J. Phys. Chem. C **115**, 8345 (2011).

[40] F. Cora, A. Patel, N. M. Harrison, R. Dovesi, and C. R. A. Catlow, An *ab initio* Hartree-Fock study of the cubic and tetragonal phases of bulk tungsten trioxide, J. Am. Chem. Soc. **118**, 12174 (1996).

[41] B. A. De Angelis and M. Schiavello, X-ray photoelectron spectroscopy study of nonstoichiometric tungsten oxides, J. Solid State Chem. **21**, 67 (1977).

[42] D. Barreca, G. Carta, A. Gasparotto, G. Rossetto, E. Tondello, and P. Zanella, A study of nanophase tungsten oxides thin films by XPS, Surf. Sci. Spectra **8**, 258 (2001).

[43] F. Bussolotti, L. Lozzi, M. Passacantando, S. La Rosa, S. Santucci, and L. Ottaviano, Surface electronic properties of polycrystalline WO_3 thin films: A study by core level and valence band photoemission, Surf. Sci. **538**, 113 (2003).

[44] J. J. Fripiat and X. Lin, Hydrogen intercalation within transition metal oxides: Entropy, enthalpy, and charge transfer, J. Phys. Chem. **96**, 1437 (1992).

[45] S. J. Kerber, J. J. Bruckner, K. Wozniak, S. Seal, S. Hardcastle, and T. L. Barr, The nature of hydrogen in x-ray photoelectron spectroscopy: General patterns from hydroxides to hydrogen bonding, J. Vac. Sci. Technol., A **14**, 1314 (1996).

[46] J. L. Bourque, M. C. Biesinger, and K. M. Baines, Chemical state determination of molecular gallium compounds using XPS, Dalton Trans. **45**, 7678 (2016).

[47] O. F. Schirmer and E. Salje, Conduction bipolarons in low-temperature crystalline WO_{3-x}, J. Phys. C: Solid State Phys. **13**, L1067 (1980).

[48] G. Hollinger, T. Minh Duc, and A. Deneuville, Charge Transfer in Amorphous Colored WO_3 Films Observed by X-Ray Photoelectron Spectroscopy, Phys. Rev. Lett. **37**, 1564 (1976).

[49] R. S. Crandall and B. W. Faughnan, Electronic Transport in Amorphous H_xWO_3, Phys. Rev. Lett. **39**, 232 (1977).

[50] V. Wittwer, O. F. Schirmer, and P. Schlotter, Disorder dependence and optical detection of the Anderson transition in amorphous H_xWO_3 bronzes, Solid State Commun. **25**, 977 (1978).

[51] A. Braun and Q. Chen, Experimental neutron scattering evidence for proton polaron in hydrated metal oxide proton conductors, Nat. Commun. **8**, 15830 (2017).

[52] W. Wang, A. Janotti, and C. G. Van De Walle, Role of oxygen vacancies in crystalline WO_3, J. Mater. Chem. C **4**, 6641 (2016).

[53] S. S. Kalanur, L. T. Duy, and H. Seo, Recent progress in photoelectrochemical water splitting activity WO_3 photoanodes, Top. Catal. **61**, 1043 (2018).

[54] J. Yan, T. Wang, G. Wu, W. Dai, N. Guan, L. Li, and J. Gong, Tungsten oxide single crystal nanosheets for enhanced multichannel solar light harvesting, Adv. Mater. (Weinheim) **27**, 1580 (2015).

[55] T. Singh, R. Müller, J. Singh, and S. Mathur, Tailoring surface states in WO_3 photoanodes for efficient photoelectrochemical water splitting, Appl. Surf. Sci. **347**, 448 (2015).

[56] S. Reich, G. Leitus, R. Popovitz-Biro, A. Goldbourt, and S. Vega, A possible 2D H_xWO_3 superconductor with a T_c of 120 K, J. Supercond. Novel Magn. **22**, 343 (2009).

[57] C. Pellegrini, H. Glawe, and A. Sanna, Density functional theory of superconductivity in doped tungsten oxides, Phys. Rev. Materials **3**, 064804 (2019).